







In the format provided by the authors and unedited.

High irradiance performance of metal halide perovskites for concentrator photovoltaics

Zhiping Wang ^{1,2}, Qianqian Lin ^{1,2}, Bernard Wenger¹, M. Greyson Christoforo¹, Yen-Hung Lin ¹, Matthew T. Klug¹, Michael B. Johnston ¹, Laura M. Herz ¹ and Henry J. Snaith ^{1*}

¹Clarendon Laboratory, Department of Physics, University of Oxford, Oxford, UK. ²These authors contributed equally: Zhiping Wang, Qianqian Lin.
*e-mail: henry.snaith@physics.ox.ac.uk

Supplementary Information

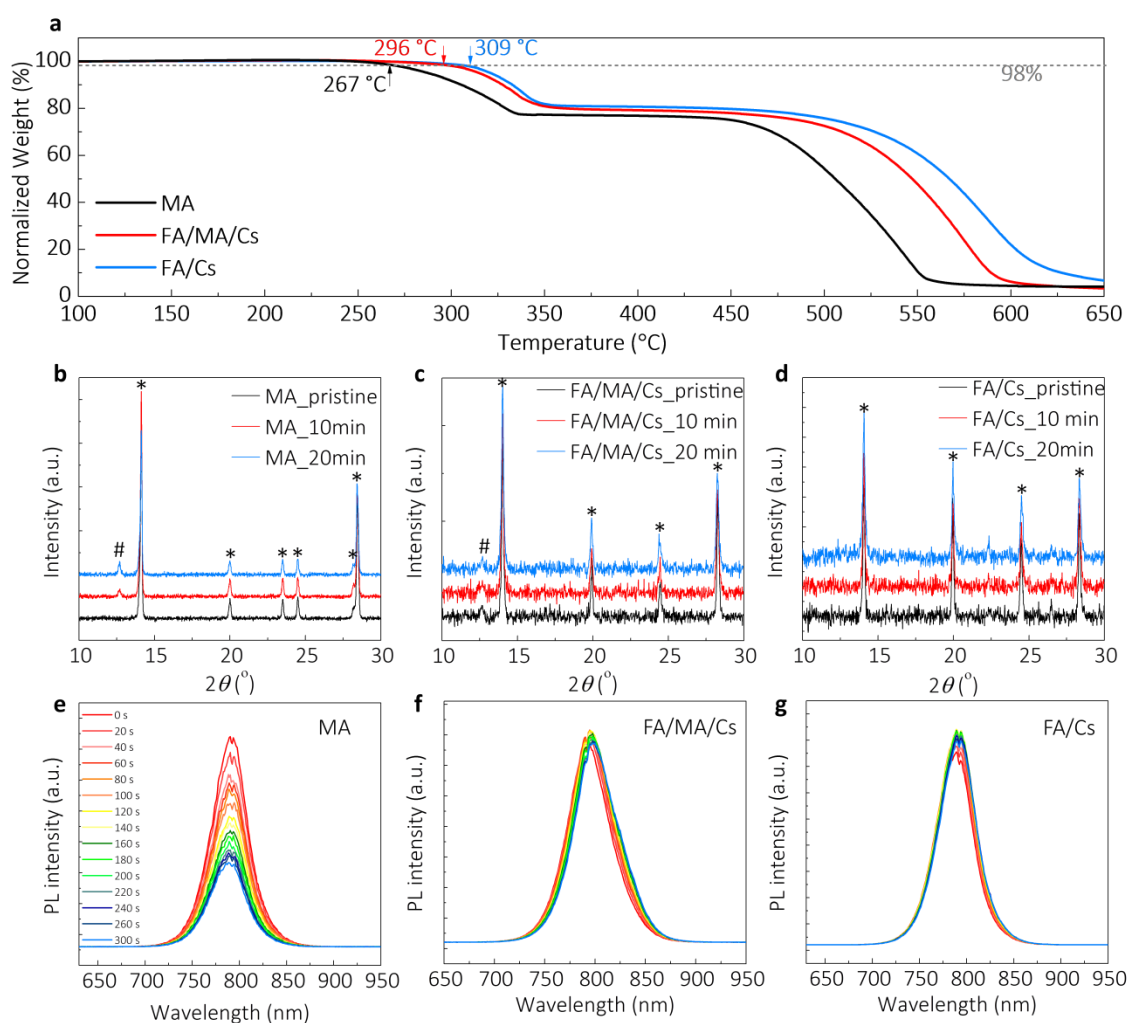
High irradiance performance of metal halide perovskites for concentrator photovoltaics

Zhiping Wang,[†] Qianqian Lin,[†] Bernard Wenger, Yen-Hung Lin, M. Greyson

Christoforo, Matthew T. Klug, Michael B. Johnston, Laura M. Herz, Henry J. Snaith*

Clarendon Laboratory, Department of Physics, University of Oxford, Parks Road, Oxford, OX1 3PU, United Kingdom

Correspondence: henry.snaith@physics.ox.ac.uk



Supplementary Figure 1 | Stability of perovskite compounds and films under heat and visible irradiance. **a**, Thermogravimetric curves of MAPbI₃ (labelled as MA), FA_{0.79}MA_{0.16}Cs_{0.05}PbI_{2.7}Br_{0.3} (labelled as FA/MA/Cs) and FA_{0.83}Cs_{0.17}PbI_{2.7}Br_{0.3} (labelled as FA/Cs) perovskite films. **b-d**, X-ray diffraction patterns of MA, FA/MA/Cs and FA/Cs perovskite films irradiated with monochromatic 532 nm light with the equivalent absorbed photon flux to 7 suns irradiance with different exposure times,

stressed and measured in ambient air. The asterisk symbol (*) denotes perovskite phases and the hash (#) denotes PbX_2 , where X is a mixture of I and Br. We note that these XRD patterns are presented on different absolute scales, and the apparent different noise levels in the spectrum are due to different absolute peak scattering intensities, and the scale at which they are presented. **e-g**, In-situ monitored PL spectra of MA, FA/MA/Cs and FA/Cs perovskite films excited by a 400 nm laser (equivalent to 10 suns absorbed photon flux) continuously for 5 mins in ambient air.

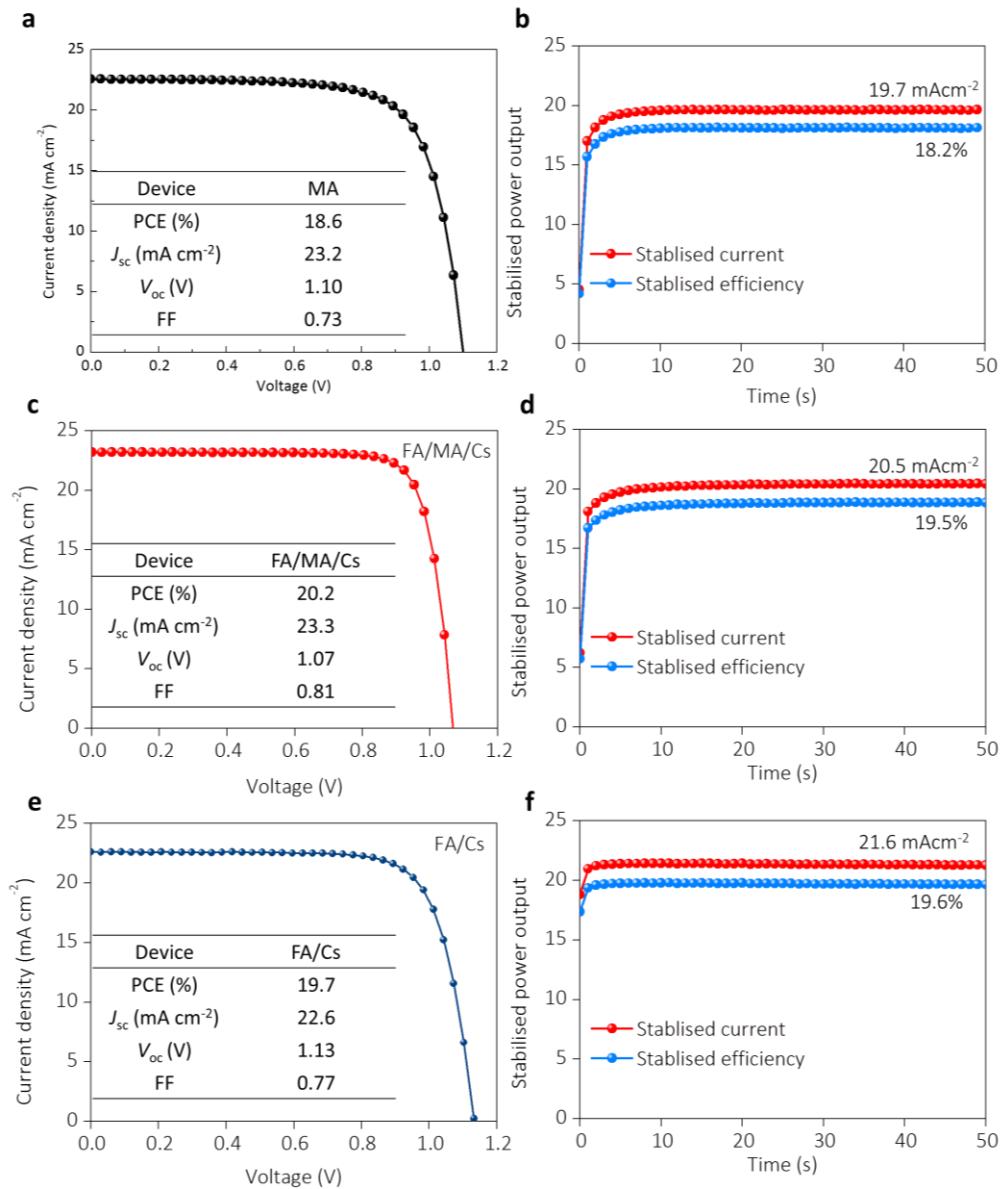
Supplementary Note 1. Material stability under high irradiance.

We start by investigating MAPbI_3 (labelled as MA), $\text{FA}_{0.83}\text{Cs}_{0.17}\text{PbI}_{2.7}\text{Br}_{0.3}$ (labelled as FA/Cs) and $\text{FA}_{0.79}\text{MA}_{0.16}\text{Cs}_{0.05}\text{PbI}_{2.7}\text{Br}_{0.3}$ (labelled as FA/MA/Cs) as representative perovskite absorber materials for CPV tests, where MA is methylammonium (CH_3NH_3^+) and FA is formamidinium $[(\text{NH}_2)_2\text{CH}^+]$. We process all the films using a conventional anti-solvent quenching spin-coating method¹. We first identify if the perovskite films can be intrinsically stable under elevated temperatures and concentrated sunlight. To determine the thermal stability of these perovskites, we perform thermogravimetric analysis on powdered perovskite samples, which we produced by scraping post cured perovskite films off their substrates. In **Supplementary Fig. 1a**, we show that the mixed cation perovskites exhibit much better stability, compared with the neat MA perovskite. We find the highest decomposition temperature for the FA/Cs perovskite, which decomposes at over 300 °C. As we show in **Supplementary Fig. 1a**, the recorded 2% weight loss temperature is 267 °C, 296 °C and 307 °C for MA, FA/MA/Cs and FA/Cs perovskites, respectively. The enhanced thermal stability by mixing Cs cation and minimizing the MA content is consistent with the recent progress on the achievements of long-term stable perovskite solar cells²⁻⁵. We also note that there is a significant shift to higher temperatures in the 2nd decomposition step, where the 2nd step is expected to be due to the sublimation of the inorganic components. This is most likely due to the presence of Cs, with a higher Cs content in the FA/Cs perovskite.

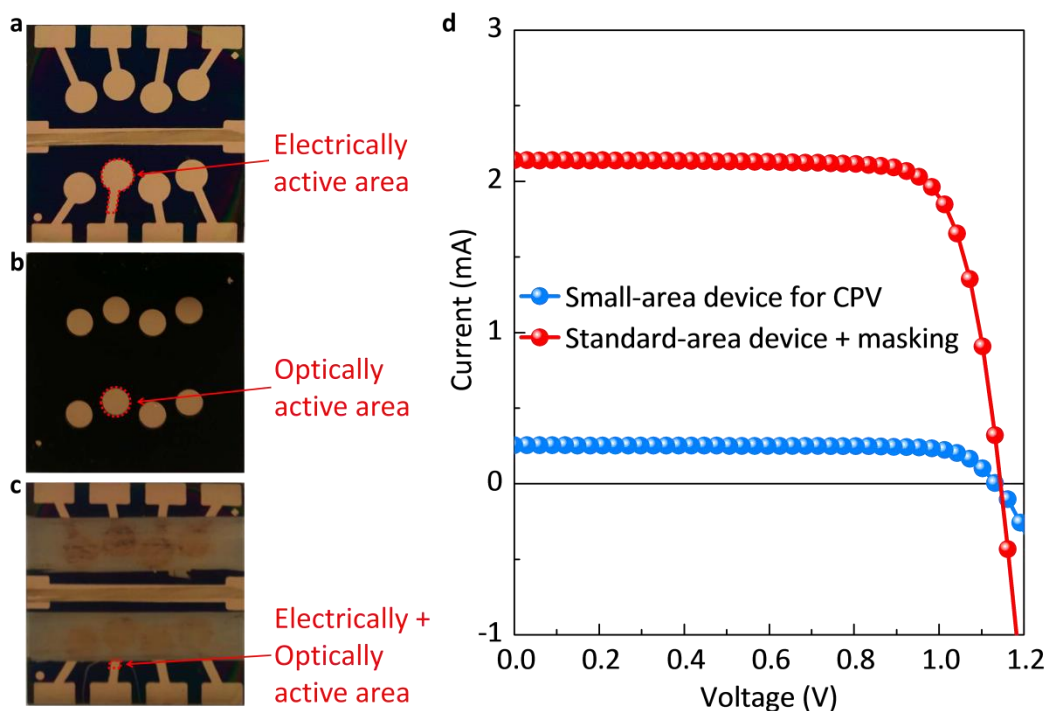
In order to assess the material stability under high intensity visible light irradiation, we monitor the changes in X-ray diffraction (XRD) and photoluminescence (PL) spectra of MA, FA/MA/Cs and FA/Cs perovskite thin-films after concentrated irradiation from monochromatic visible light. From the XRD spectra (**Supplementary Fig. 1b-d**), we confirm that all pristine films crystallize into the expected perovskite phases. Upon continuous monochromatic light exposure at equivalent to 7 suns, we observe the lead iodide (PbI_2) diffraction at around $2\theta = 12.6^\circ$ to emerge in the MA films. We concomitantly observe the PbI_2 peak to increase while the (100) perovskite peak ($2\theta = 14.1^\circ$) decreases with increasing exposure time, consistent with decomposition of the MAPbI_3 perovskite. For the FA/MA/Cs we already observe the presence of PbX_2 peak (X is a mixture of I and Br) before exposure to light, but we do

not observe this peak to grow considerably over this exposure time. For the FA/Cs perovskite films, we do not observe the presence of PbX_2 , nor obvious changes in the perovskite phase reflections, which indicates enhanced structural stability. We record the in-situ PL spectra of these perovskite films to elucidate the evolution of radiative recombination, which is a key property for high quality optoelectronic materials. We clearly observe a fast attenuation in PL intensity for the MA sample (**Supplementary Fig. 1e**), which most likely originates from the decomposition of the perovskite films, as suggested by the XRD measurement. We also note that light absorbed in the increasing fraction of PbI_2 may not contribute so strongly to photoluminescence. Comparatively, changes in the PL spectra and intensity for the FA/MA/Cs and FA/Cs films are negligible (**Supplementary Figs. 1f and g**). Previous works, including ours, pointed out that a fundamental issue with the MA-based perovskite is the relative volatility of MA, which evolves out of the film during heating⁴⁻⁷. When we illuminate the film with intense light, photon-induced heating may result in the volatile MA leaving the film⁸⁻¹⁰. In addition, photo-induced charge generation under sunlight and in the presence of oxygen, has previously been shown to generate electrons in the perovskite that react with oxygen to produce superoxide, which rapidly decomposes the methylammonium iodide into methylamine and HI^{11,12}. In contrast, the FA/MA/Cs and FA/Cs composite perovskites reveal much better photo-stability, which is in agreement with the lower volatility of the cations, and also suggests that the FA and Cs cations are less susceptible to the superoxide degradation path¹³. From our analysis above, it appears that the FA/MA/Cs and FA/Cs perovskites are the most promising materials for CPV applications.

We investigate the performance of PV cells employing the different perovskite compositions under range of intensities of monochromatic light and present our findings in the **Supplementary Notes 2 and 3**, and **Supplementary Figs. 2-6**. Our concluding observation is that the perovskite PV cells employing the FA/Cs perovskite absorber are more efficient and more stable under high intensity irradiance, and we hence proceed to focus on this FA/Cs composition for the remainder of our study.



Supplementary Figure 2| Device performances under simulated AM 1.5G 100 mW cm^{-2} irradiance. **a**, Current-density voltage (J – V) characteristics of the perovskite solar cells using MA photoactive layers, measured from forward bias to short-circuit under simulated 1 sun AM 1.5G (100 mW cm^{-2}) irradiance. **b**, Corresponding stabilised power output of the MA cells. **c**, J – V characteristics of the FA/MA/Cs perovskite solar cells. **d**, Corresponding stabilised power output of the FA/MA/Cs cells. **e**, J – V characteristics of the FA/Cs perovskite solar cells. **f**, Corresponding stabilised power output of the FA/Cs cells. We obtain the stabilised power output by holding the cell at a fixed voltage near the maximum power point on the J – V curve for 50 s.



Supplementary Figure 3| Device area and masking condition. **a**, Standard-area device without masking. The red dotted line highlights the electrically active area. **b**, Standard-area device without masking. The red dotted line highlights the optically active area, which is 0.0919 cm^2 . **c**, Scratched small-area device. The red dotted line highlights the electrically plus optically active area. **d**, Current-voltage characteristics of the masked standard-area device and the scratched small-area device, measured from forward bias to short-circuit under simulated 1 sun AM 1.5 G (100 mW cm^{-2}) irradiance. The current values for the standard-area device and the small-area device are 2.14 and 0.25 mA, respectively.

Supplementary Note 2. Impacts of perovskite composition on high-irradiance performances.

We now proceed to test the perovskite absorber layers integrated into complete solar cells and systematically investigate their device performance as a function of light intensity. We fabricated devices based on an n-i-p planar heterojunction architecture (glass/FTO/SnO₂/perovskite/spiro-OMeTAD/Au). We show the device characteristics measured under simulated AM 1.5 G 100 mW cm^{-2} irradiance (*i.e.* 1 sun) in **Supplementary Fig. 2**. The device masking condition and a comparison of current-voltage characteristics of as-prepared standard-area and small-area devices are shown in **Supplementary Fig. 3**. In **Supplementary Fig. 4** we show the evolution of the J_{sc} , V_{oc} , FF and PCE of the perovskite solar cells with increasing monochromatic 532 nm illumination intensity, up to the equivalent absorbed photon flux of up to 100 suns (methods described in **Supplementary Note 3**), and present the corresponding J - V

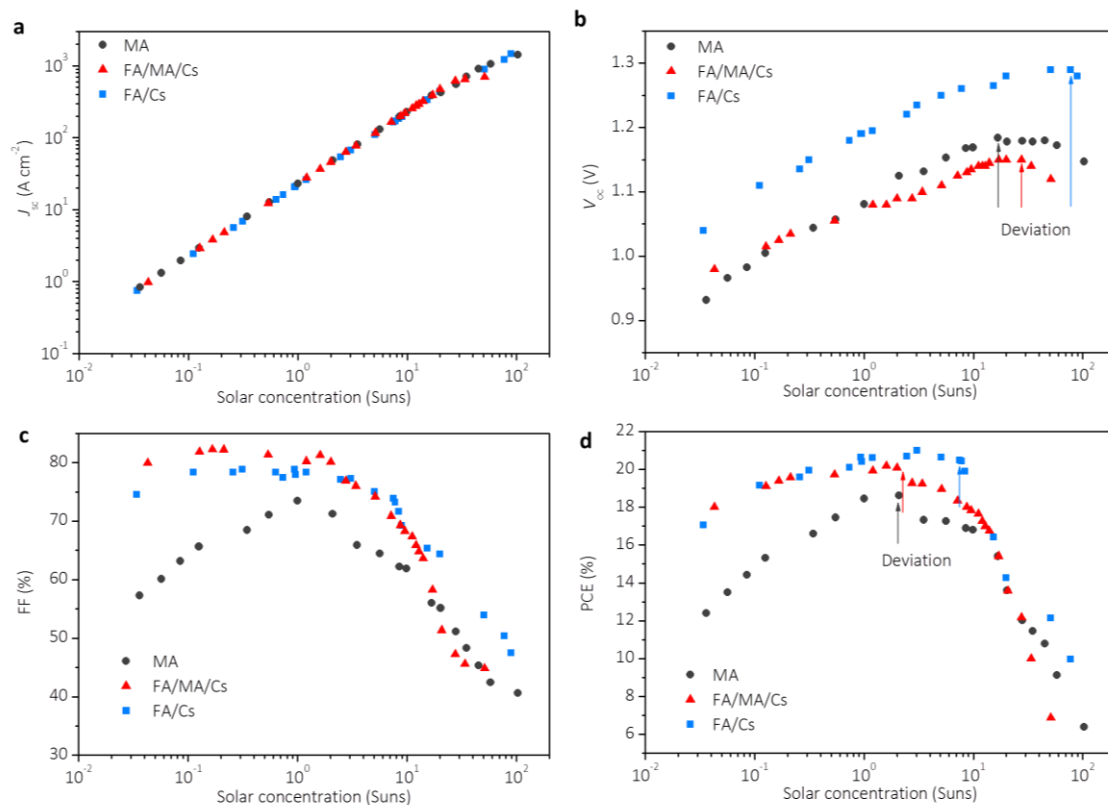
curves in **Supplementary Fig. 5**. We note that to “simulate” the concentrated light irradiation, we employed a 532 nm green laser and control the intensity with neutral density filters. We define 1 sun as the condition when the equivalent absorbed photon flux in our solar cells is identical to that achieved under AM 1.5 G 100 mW cm⁻² illumination. The J_{sc} of all devices increases linearly with increasing concentration until around 30 suns, then it starts to increase sub-linearly (**Supplementary Fig. 4a**). The linear region indicates a negligible current loss induced by the increase of light intensity. For the V_{oc} –suns relationship (**Supplementary Fig. 4b**), we observe a logarithmic increase in the V_{oc} with increasing light intensity at up towards ten sun intensity. However, the gradient of the exponent does vary between cells, with MA, FA/MA/Cs and FA/Cs increasing 100, 60 and 80 mV/decades respectively, analogous to single diode “ideality factors” of 1.7, 1.0 and 1.3 respectively¹⁴ Upon further increasing the irradiance levels, we observe a deviation of V_{oc} to the expected logarithmic monotonic increase, with the deviation commencing at 15, 30 and 80 suns for the MA, FA/MA/Cs and FA/Cs device, respectively.

Despite the monotonic increase in both V_{oc} and J_{sc} with increasing light intensity, we observe that the FF of all devices decreases at much lower irradiance levels than the point at which the V_{oc} saturates. We find that all cells lose FF at around 1.6 suns, with a 20% relative drop. As a result, the PCE starts to decrease at only 1.2 suns for the MA perovskite device and at 2 suns for the FA/MA/Cs perovskite device (**Supplementary Fig. 4d**). In addition, we do not see any obvious increase in the PCE as compared to its 1-sun efficiency for the devices with these perovskite compositions. In contrast, we observe an increase in PCE until around 8 suns for the FA/Cs device, mainly due to the continuous increase in V_{oc} which overcompensates for the drop in FF.

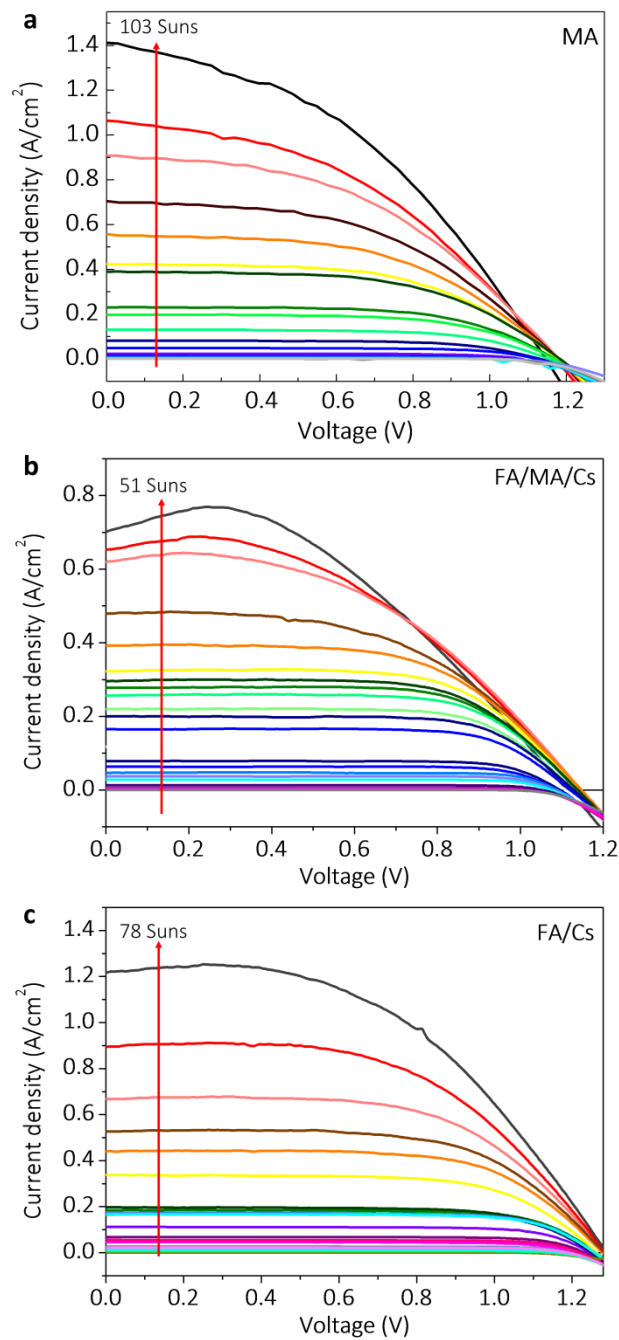
To further assess the stability of these devices under high irradiance, we measured the V_{oc} of the perovskite devices under continuous 5 suns irradiance, which we show in **Supplementary Fig. 6**. We observe that the MA and FA/MA/Cs perovskite devices exhibit a fast decay in V_{oc} , while we observe a stable V_{oc} of the FA/Cs device. We attribute the V_{oc} decay of the MA device to the decomposition of MAPbI₃ into PbI₂ at high concentrations, as indicated in the spectroscopic study, which we presented in **Supplementary Figs. 1a, b** and **e**. We do not observe any obvious decomposition of the FA/MA/Cs film under similar concentration of irradiance according to both our XRD (**Supplementary Fig. 1c**) and PL (**Supplementary Fig. 1f**) analysis under similar light intensity exposure; however we still observe a relatively rapidly decaying V_{oc} , for the FA/MA/Cs device. We therefore expect that this is due to the generation of non-radiative recombination sites near or at the charge extraction interfaces, which would not show up in XRD and would not necessarily be present in the isolated perovskite films upon which we performed our PL measurements.

We note that it has been previously observed that photo-excitation can result in halide

segregation into iodide-rich and bromide-enriched domains, with the iodine-rich domains comprising a lower band gap, which is expected to reduce the V_{oc} of the solar cells¹⁵. At high concentration irradiance, such halide segregation should be more pronounced however, the consistent and stable V_{oc} of the FA/Cs device is consistent with halide segregation not occurring, and not diminishing V_{oc} in with this mixed-anion composition, which contains approximately 10% Br.



Supplementary Figure 4| CPV device performances under monochromatic green laser light. Comparison of **a**, J_{sc} , **b**, V_{oc} , **c**, FF, and **d**, PCE of perovskite solar cell devices measured under various solar concentration factors (up to 100 suns illumination), measured with a two-wire connections configuration. MA, FA/MA/Cs and FA/Cs represent devices with $MAPbI_3$, $FA_{0.79}MA_{0.16}Cs_{0.05}PbI_{2.7}Br_{0.3}$ and $FA_{0.83}Cs_{0.17}PbI_{2.7}Br_{0.3}$ perovskite photoactive layers, respectively. Illumination was with a 532 nm monochromatic laser and the relative solar irradiance is calculated as the equivalent absorbed flux in comparison to AM 1.5G $100\ mW\ cm^{-2}$ irradiance. All measurements are performed on unsealed cells in ambient air. The active cell area was $\sim 1\ mm^2$, in order to reduce parasitic series resistance losses.



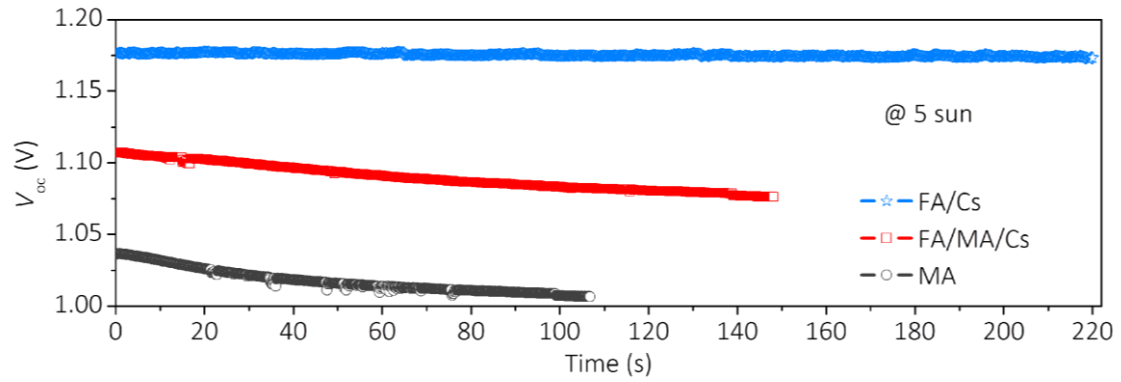
Supplementary Figure 5| Performances of perovskite cells under concentrated light. Measured J - V characteristics of perovskite solar cells based on (a) MA, (b) FA/MA/Cs and (c) FA/Cs perovskite at various light intensities under 532-nm green laser illumination.

Supplementary Note 3. Current–Voltage measurements under simulated concentrated light (532 nm monochromatic laser light)

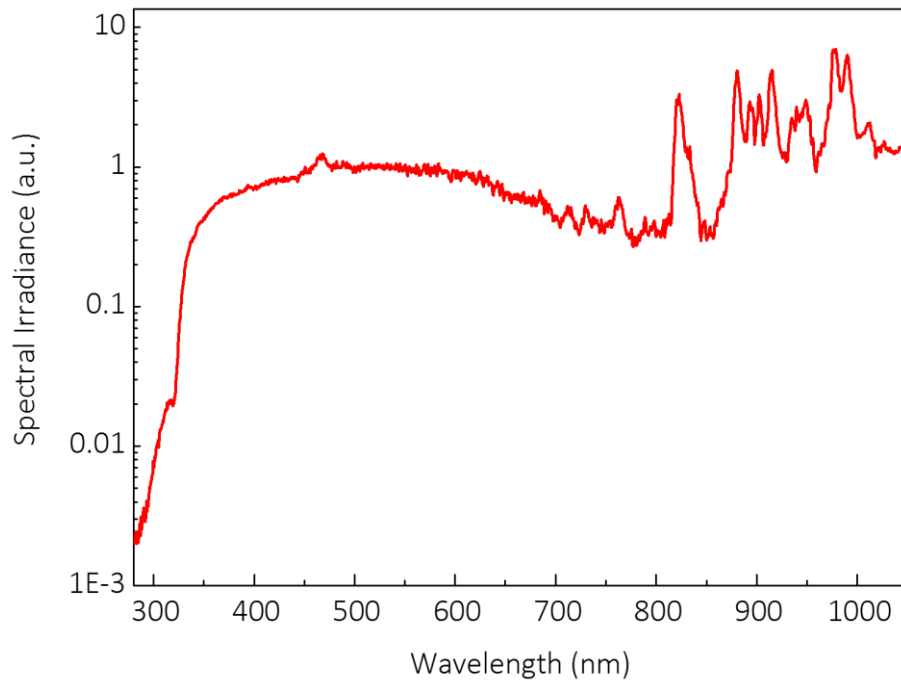
The homogenous concentrated light source was obtained via enlarging a green (532 nm) laser spot with a lens and an aperture. The light intensity was modulated by a set of neutral density filters and the relative intensity was carefully calibrated with a power meter. In order to achieve the same charge carrier concentration and short-circuit current density, less intensity from a 532 nm monochromatic light source is required than for AM 1.5G light source, since the cells have much higher EQE ($\sim 90\%$) value over the entire range of the light source. The effectivity power to current conversion can be simply defined as responsivity (R)

$$R = \frac{J}{P_{in}} = EQE \frac{q}{hf}$$

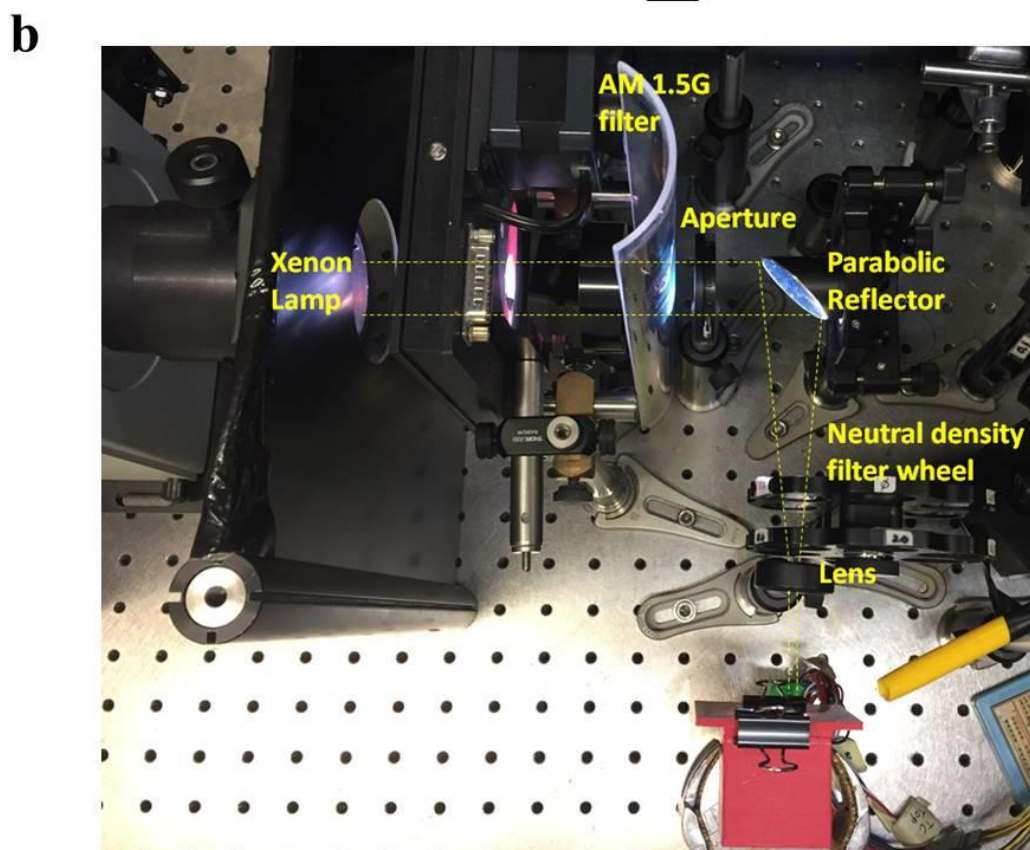
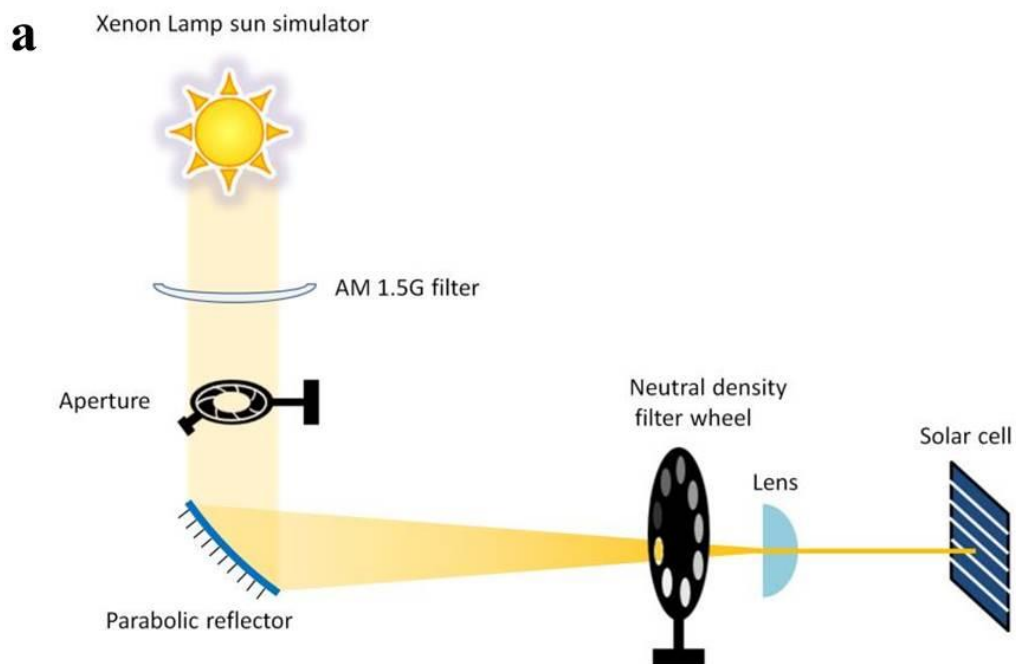
where q is the elementary charge, h is Planck's constant, f is frequency and λ is the wavelength. For example, the overall responsivity of the champion FA/Cs perovskite solar cell at 1 sun AM 1.5G illumination (R_{white}) is 0.223 A W^{-1} , while the responsivity under 532 nm green laser (R_{green}) is 0.386 A W^{-1} . Hence, 100 mW cm^{-2} AM 1.5G white light is required to achieve $22.3 \text{ mA cm}^{-2} J_{sc}$, but only 57.8 mW cm^{-2} of 532 nm green light irradiance is required to achieve the same J_{sc} , which is the 1 sun equivalent power density of the 532 nm green light source. Then, the sun concentration of the green laser is calculated based on the equivalent 1 sun power density. In fact, the absolute PCE of a solar cell under 532 nm monochromatic light will be also much higher than the value obtained from AM 1.5G test. For comparison, equivalent PCE (PCE_{eq}) was inferred from the real measured PCE_{green} under 532 green laser, corrected with a factor of R_{white}/R_{green} . The PCE_{eq} could reflect the real PCE under white illumination.



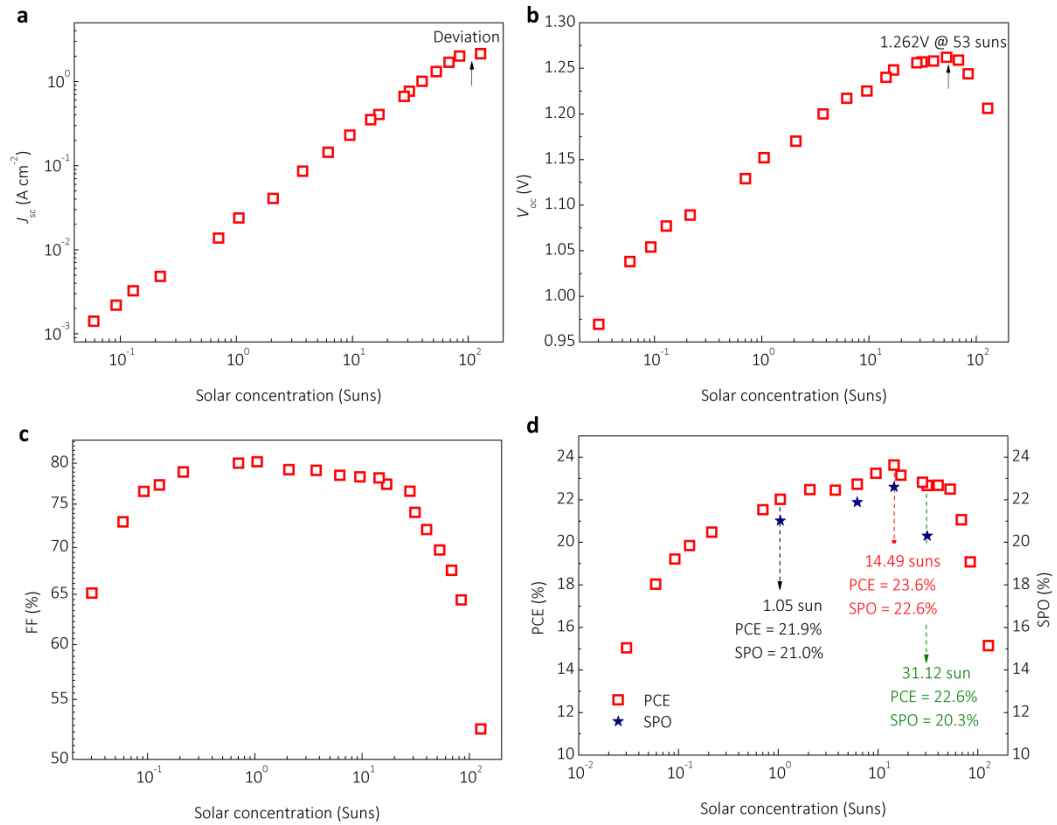
Supplementary Figure 6 | Stability under concentrated light. Tracking of the V_{oc} of the perovskite devices under 5 suns concentration. Illumination was with a 532 nm monochromatic laser and the relative solar irradiance is calculated as the equivalent absorbed flux in comparison to AM1.5 100 mWcm^{-2} irradiance. All measurements are performed on unsealed cells in ambient air. The active cell area was $\sim 1 \text{ mm}^2$, in order to reduce parasitic series resistance losses.



Supplementary Figure 7 | Spectrum of the AM 1.5G filter corrected xenon lamp light (without an OD filter).



Supplementary Figure 8| Experimental setup for device measurement under concentrated sunlight. a, Schematic illustration and b, optical photo of testing perovskite solar cells under concentrated white light illumination.



Supplementary Figure 9 | CPV performance of the champion perovskite solar cell.

Comparison of (a) J_{sc} , (b) V_{oc} , (c) FF, and (d) PCE of the champion perovskite solar cell devices measured under various solar concentration factors (up to 128 suns irradiance). The cell structure is glass/FTO/SnO₂/FA_{0.83}Cs_{0.17}PbI_{2.7}Br_{0.3}/spiro-OMeTAD/Au. All the light intensity measurements are performed on unsealed cells in ambient air under a 4-wire, source and sense mode. The active cell area was 0.82 mm², in order to reduce parasitic series resistance losses.

Supplementary Note 4. Estimation of dominating modes for charge recombination for the MA and FA/Cs perovskites.

Considering light absorption and charge recombination, the rate of change of charge density in the perovskite film is governed by the following rate equation¹:

$$\frac{dn}{dt} = G - nk_1 - n^2k_2 - n^3k_3 \quad (1)$$

where G is the charge-density generation rate, k_1 the monomolecular charge-recombination rate, k_2 the bimolecular electron–hole recombination rate constant, and k_3 the Auger recombination rate constant.

Under open-circuit conditions in a solar cell the charge density is constant, and therefore under this steady state condition $dn/dt = 0$. We can therefore consider,

$$G = nk_1 + n^2k_2 + n^3k_3. \quad (2)$$

For all perovskite films studied so far, under AM 1.5G, $k_1 \gg k_2n \gg k_3n^2$, therefore under low light levels, recombination is governed by monomolecular recombination, under intermediate illumination intensity, recombination is governed by bimolecular band-to-band recombination and under high intensity recombination is governed by 3rd order Auger recombination. We can therefore define the precise conditions associated with the transition from monomolecular to bimolecular recombination, through the charge-carrier density n_{bi} and generation rate G_{bi} , and from bimolecular to Auger recombination through n_{Auger} and G_{Auger} , as being the points when the total rates for mono and bimolecular recombination, and bimolecular and Auger recombination equal each other. These conditions are satisfied when,

$$n_{bi}k_1 = n_{bi}^2k_2, \quad (3)$$

and

$$n_{Auger}^2k_2 = n_{Auger}^3k_3 \quad (4)$$

Therefore,

$$n_{bi} = \frac{k_1}{k_2} \quad (5)$$

and

$$n_{Auger} = \frac{k_2}{k_3} \quad (6)$$

and

$$G_{\text{bi}} = n_{\text{bi}}k_1 + n_{\text{bi}}^2k_2 + n_{\text{bi}}^3k_3 \quad (7)$$

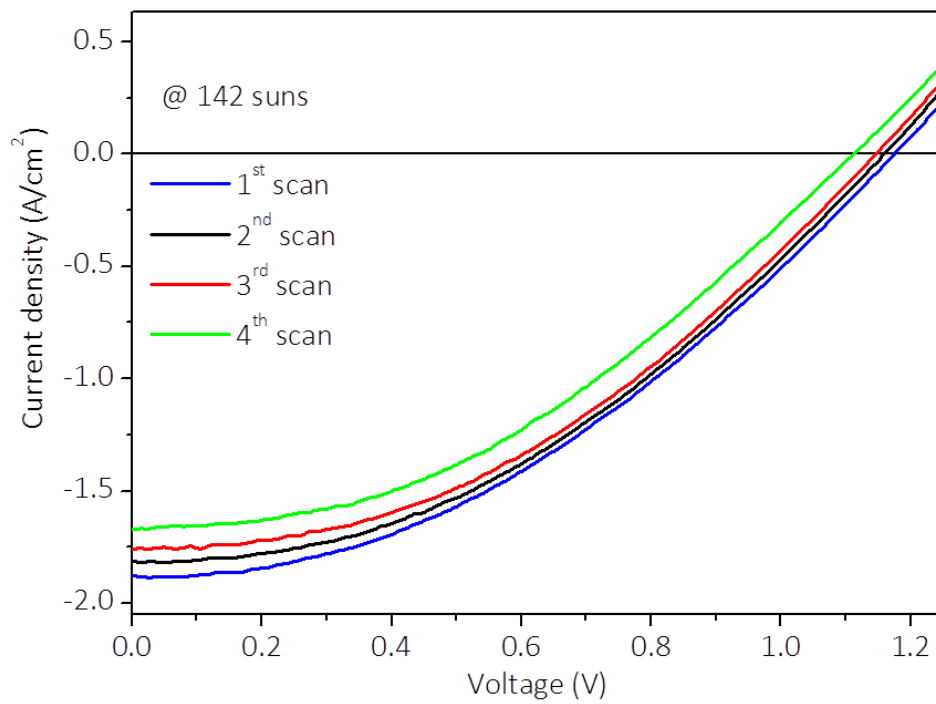
and

$$G_{\text{Auger}} = n_{\text{Auger}}k_1 + n_{\text{Auger}}^2k_2 + n_{\text{Auger}}^3k_3 \quad (8)$$

We can also relate these corresponding threshold charge generation rates for transitions between regimes (G_{bi} and G_{Auger}), to the charge generation rate under 1 sun illumination, in order to determine the equivalent solar concentration (C) we would expect to have to achieve in order to transition between these different regimes as $C_{\text{bi/Auger}} = G_{\text{Bi/Auger}}/G_{1\text{sun}}$. We have calculated $G_{1\text{sun}}$ by integrating the spectral response of the solar cell over the 100 mWcm⁻² AM 1.5G solar spectrum and determine a value of $G_{1\text{sun}} \sim 3.1 \times 10^{21} \text{ cm}^{-3} \text{ s}^{-1}$, with an active layer thickness of 500 nm. In the table below we tabulate the recombination rate constants and n , G and C for Bimolecular and Auger regimes.

Supplementary Table 1. Summary of threshold conditions where transitions between regimes occur for MAPbI₃ and FA_{0.83}Cs_{0.17}PbI_{2.7}Br_{0.3} perovskites. The monomolecular recombination rate constant (k_1), bimolecular recombination rate constant (k_2) and Auger recombination rate constant (k_3) of the MAPbI₃ and FA_{0.83}Cs_{0.17}PbI_{2.7}Br_{0.3} perovskites are extracted from Supplementary Refs. 2 and 3, respectively.

	MAPbI₃	FA_{0.83}Cs_{0.17}PbI_{2.7}Br_{0.3}
$k_1 [\text{s}^{-1}]$	15×10^6	5×10^6
$k_2 [\text{cm}^3 \text{ s}^{-1}]$	0.6×10^{-10}	0.2×10^{-10}
$k_3 [\text{cm}^6 \text{ s}^{-1}]$	1.6×10^{-28}	0.2×10^{-28}
$n_{\text{bi}} [\text{cm}^{-3}]$	0.25×10^{18}	0.25×10^{18}
$G_{\text{bi}} @ V_{\text{oc}} [\text{cm}^{-3} \text{ s}^{-1}]$	1×10^{25}	2.81×10^{24}
$C_{\text{bi}} (\text{Suns})$	3230	230
$n_{\text{Auger}} [\text{cm}^{-3}]$	0.38×10^{18}	1×10^{18}
$G_{\text{Auger}} @ V_{\text{oc}} [\text{cm}^{-3} \text{ s}^{-1}]$	2.25×10^{25}	4.5×10^{25}
$C_{\text{Auger}} (\text{Suns})$	7000	14000



Supplementary Figure 10 | *J-V* scans of a FA/Cs perovskite solar cell under monochromatic 532 nm green light at 142 suns.

Supplementary Note 5. Ideality factor estimations from light J - V curves.

Comparing to ideality factor from the intensity dependence of the V_{oc} , as described in **Supplementary Note 1**, the ideality factor estimated using the entire light JV curve (not just the value of V_{oc}) increases constantly with increasing light intensity. We show the calculation and resultant ideality factors as a function of light intensity in **Supplementary Figure 10**. An ideality factor estimated to be above 2 has no real physical meaning. The high ideality factor is required to fit the “soft” kink in the JV curve near maximum power point. We do note that high ideality factors have been estimated before for perovskite solar cells¹⁶. We expect that is related to the hysteresis and ionic effects in perovskite solar cells, which do still influence the shape of the JV curves. This is clearly something which does warrant significant further investigations. It is apparent that the “ideality factor” for perovskite solar cells is either not a good fitting factor to employ, or the reasons for deviation from expectations need to be understood, the impact of them understood for power generation, and if a negative impact, methods to bring the ideality factor back into the normal range with physical meaning. However, since this specific aspect clearly requires unique, in-depth studies, and will be a study in its own right, we have removed comments concerning the ideality factor estimations from manuscript.

Diode ideality factors were found by fitting specific regions of the solar cell J - V curves to the non-ideal characteristic equation for a single junction solar cell:

$$I = I_L - I_0 \left\{ \exp \left[\frac{q(V + IR_S)}{nkT} \right] - 1 \right\} - \frac{V + IR_S}{R_{SH}}$$

Where I is the current through the device (amperes, measured),

I_L is the photogenerated current contribution (amperes),

I_0 is the diode’s reverse saturation current in (amperes),

q is the elementary charge in (coulombs),

V is the voltage across the device (volts, measured),

R_S is the series resistance in (ohms),

n is the diode’s ideality factor (unitless),

k is Boltzmann’s constant (Joules per degree Kelvin),

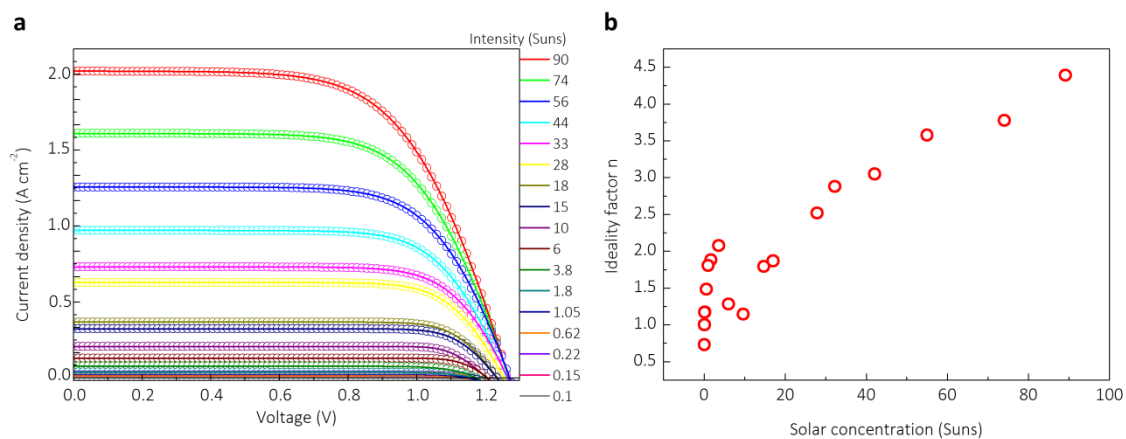
T is the device’s temperature (degrees Kelvin),

and

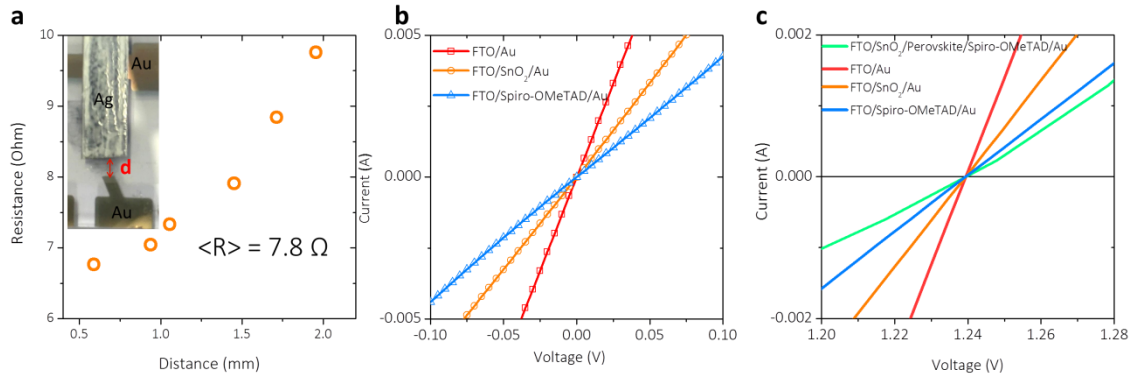
R_{SH} is the shunt resistance (ohms).

Fitting was done using the bounded, non-linear least-squares Levenberg–Marquardt error minimization method as implemented in the `lmfit` python software package¹⁷ using a custom fitting program¹⁸. I, V, q and k are known (or experimentally measured) inputs to the system, I_L, I_0, R_S, n and R_{SH} are fit parameters and T is assumed to be

29 degrees Celsius.



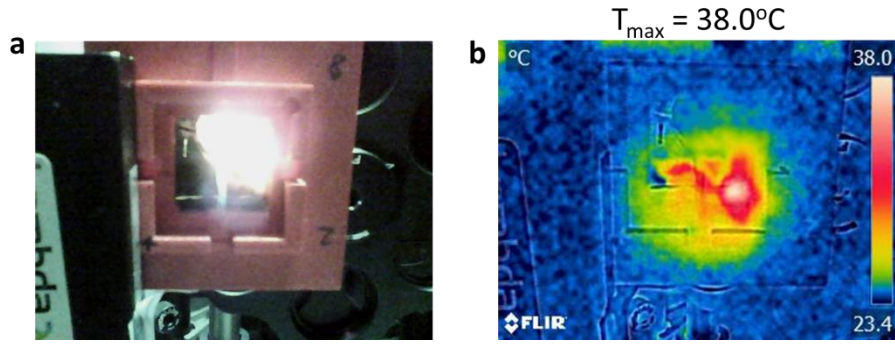
Supplementary Figure 11 | Estimation of ideality factor. a, Fitting curves (solid line) of the JV data (symbol) of perovskite device with a spiro-OMeTAD hole transporting layer, measured at various solar concentrations. b, Corresponding ideality factors extracted from the fitted curves.



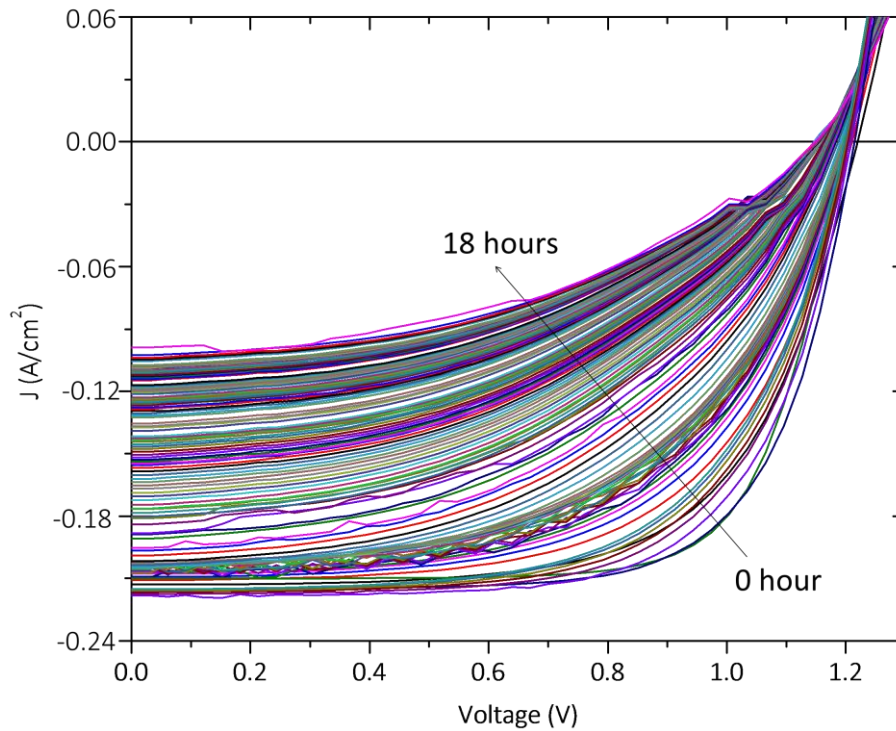
Supplementary Figure 12| Quantifying the contribution of series resistance from each component in the solar cell: a, Measurement and estimation of FTO resistance in the complete device. The resistance of FTO is measured as a function of the distance, d , between the gold electrode and the silver conductive tape, as shown in the inset. If the series resistance in this cell is dominated by the resistance through the FTO, the contribution of the resistance ($\langle R \rangle$) from the FTO electrode in a complete solar cell device can be approximately expressed as: $\langle R \rangle = \frac{\int_{x_1}^{x_2} R dx}{x_2 - x_1}$, where x is the distance from the conductive adhesive to the edge of the Au electrode, and R is the measured resistance value. **b,** Measured current-voltage characteristics of FTO/SnO₂/Au and FTO/spiro-OMeTAD (doped with Li-TFSI and *t*BP at the same concentration as used in the PV cells)/Au. For reference, an FTO/Au characteristic is included with a slope corresponding to $\langle R \rangle$ determined in (a). **c,** Comparison of the current-voltage characteristic of the measured interlayer devices and the perovskite devices measured at 15 suns. For reference, an FTO/Au characteristic is included with a slope corresponding to $\langle R \rangle$ determined in (a). The corresponding resistance values are listed in **Supplementary Table 2.**

Supplementary Table 2. Series resistance of the interlayers extracted from Supplementary Figure 11. The resistance for the full device under 15 suns was taken from slope of J - V curve at V_{oc} .

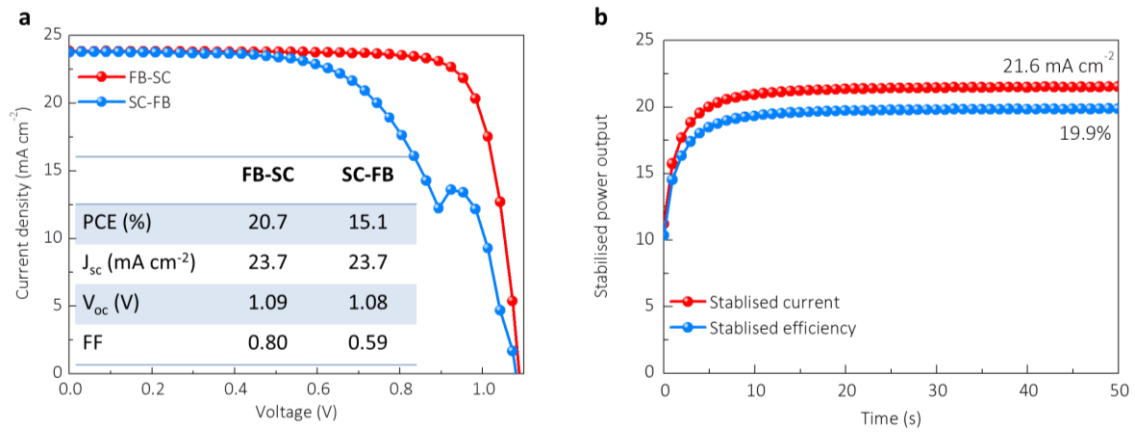
	Full device under 15 suns	FTO ($\langle R \rangle$)	SnO₂ + FTO	Spiro-OMeTAD + FTO	SnO₂ + Spiro-OMeTAD + FTO (estimated)
Resistance (Ω)	31 ± 0.05	7.8 ± 0.09	15.2 ± 0.001	24.8 ± 0.001	32.2 ± 0.01



Supplementary Figure 13 | **a**, Optical photograph of perovskite solar cells under concentrated white light. **b**, Simultaneously measured device surface temperature. The temperature was measured by an infrared camera from the gold electrode side of a solar cell device while the concentrated sunlight (~ 128 suns) irradiates from the glass/FTO side. We kept the light irradiates for 5 mins to obtain a stabilized temperature value. All the measurement was carried out in ambient air on non-encapsulated devices.

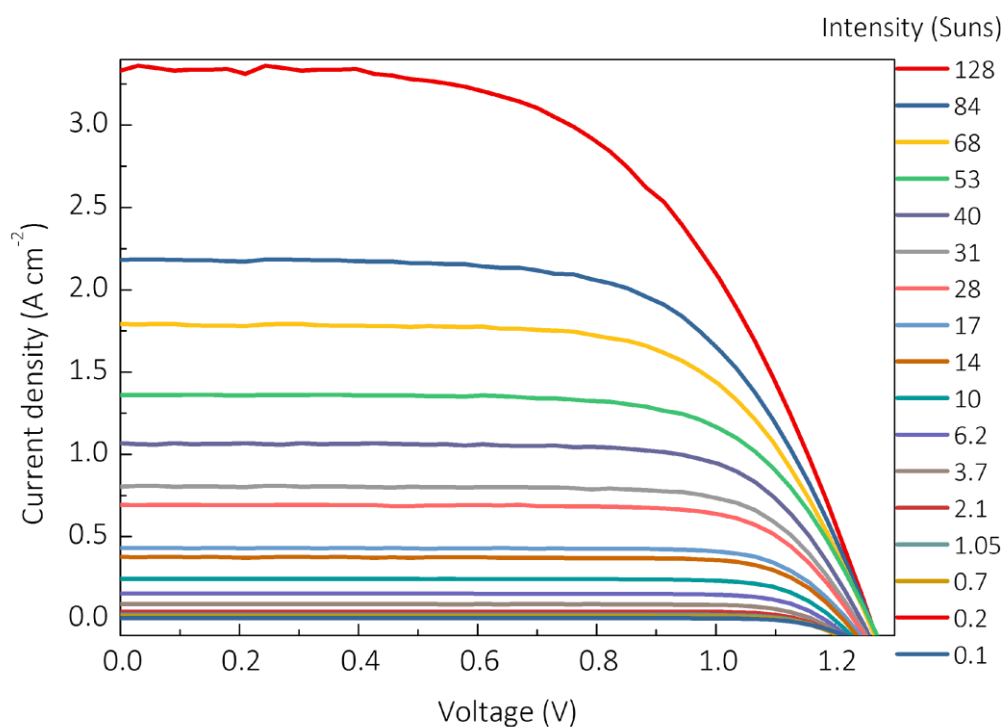


Supplementary Figure 14 | Stability of FA/Cs perovskite device with Spiro-OMeTAD as a hole transporting layer measured under 10 sun concentration. The device structure is FTO/SnO₂/FA_{0.83}Cs_{0.17}PbI_{2.7}Br_{0.3}/spiro-OMeTAD (doped with Li-TFSI and *t*BP)/Au. Illumination was with a 532 nm monochromatic laser and the relative solar irradiance is calculated as the equivalent absorbed flux in comparison to AM 1.5 G 100 mW cm⁻² irradiance. The device was held at open-circuit during ageing, and tested at different time intervals. All measurements are performed on unsealed cells in ambient air. The active cell area was ~1 mm², in order to reduce parasitic series resistance losses.

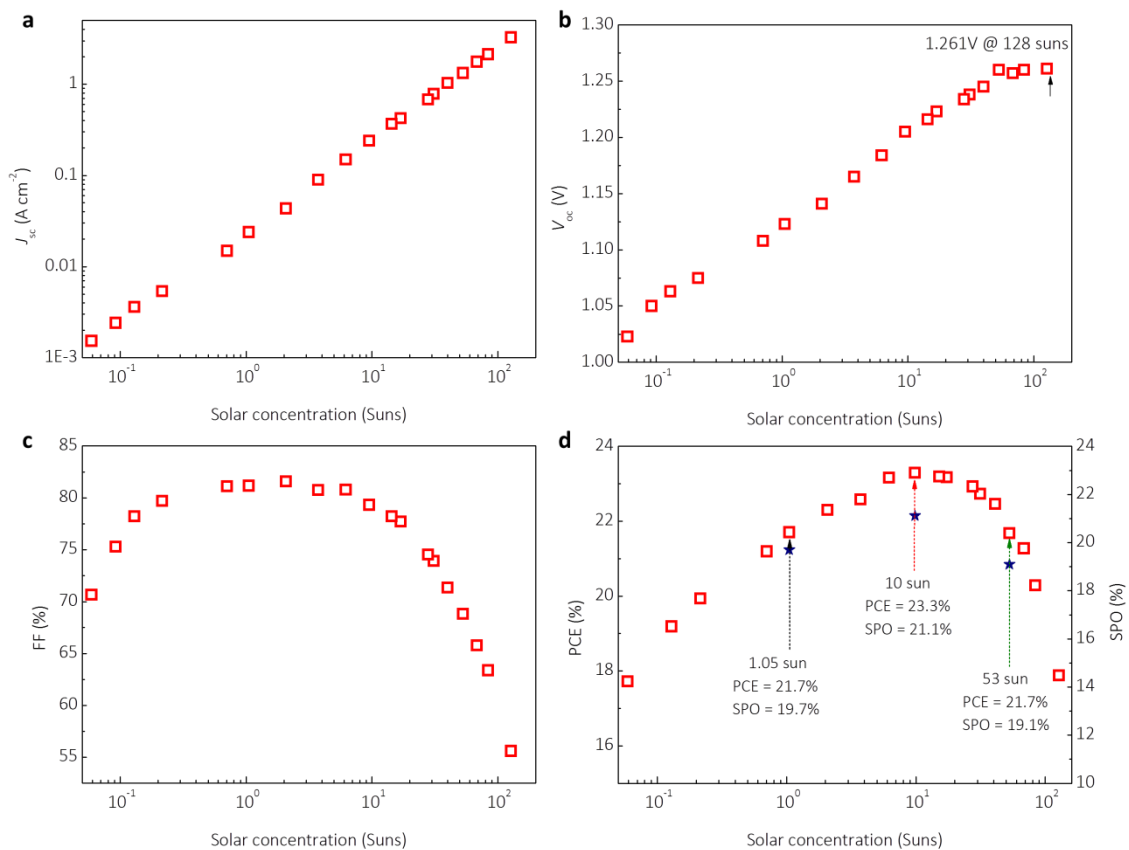


Supplementary Figure 15 | Device performance with PTAA hole transporting layer.

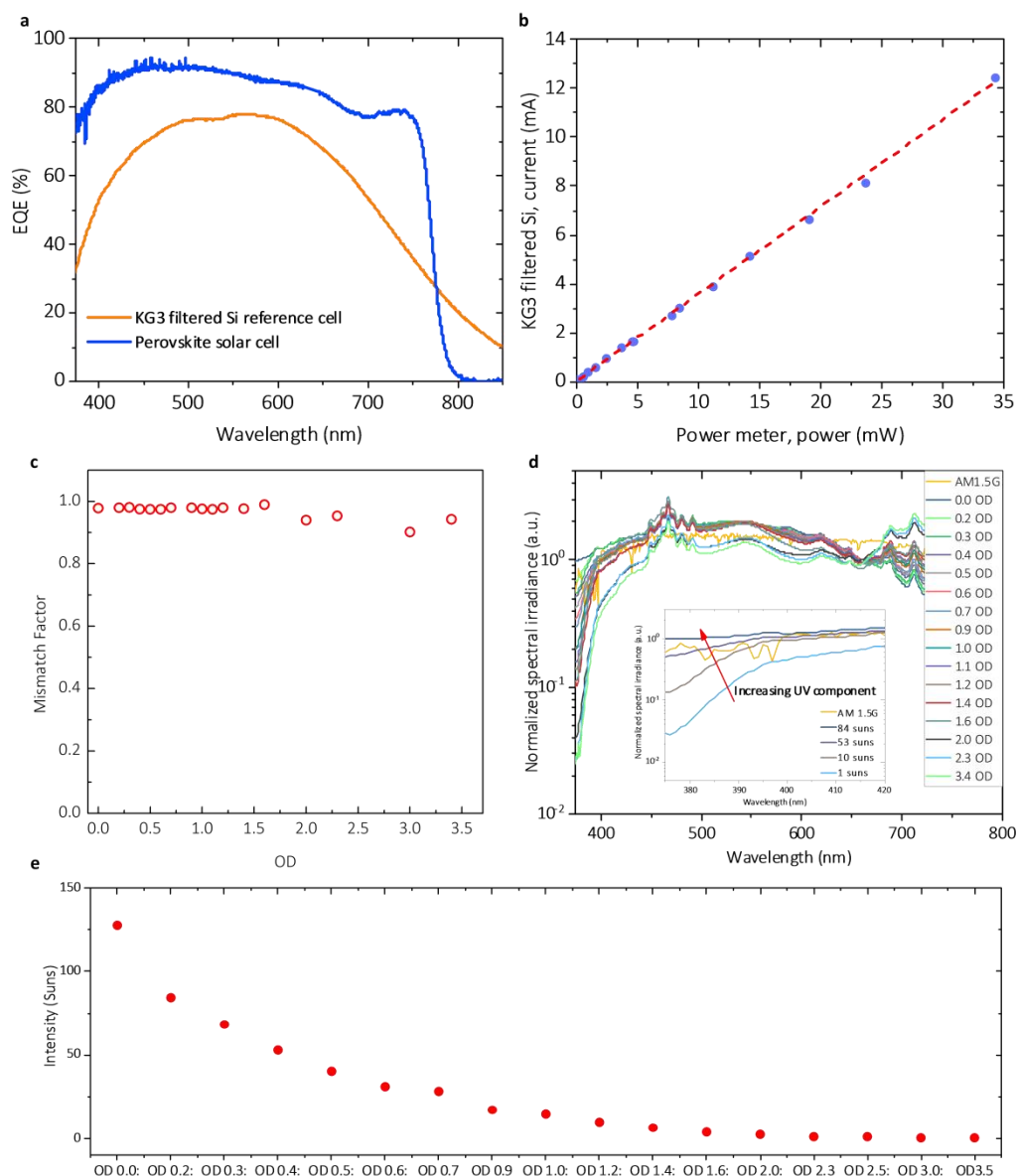
a, J - V characteristics, measured from forward bias (FB) to short-circuit (SC) and back again under simulated AM 1.5G (100 mW cm^{-2}) irradiance (1 sun). The device characteristics are described in the inserted table. **b**, Corresponding stabilised power output.



Supplementary Figure 16| Measured J - V characteristics of a device with PTAA hole transporting layer at various light intensities under concentrated white sunlight. Illumination was with a xenon lamp simulated full spectrum AM 1.5G. All the light intensity measurements are performed on sealed cells in ambient air under a 4-wire, source and sense mode. The active cell area was 0.87 mm^2 , in order to reduce parasitic series resistance losses.



Supplementary Figure 17 | Comparison of (a) J_{sc} , (b) V_{oc} , (c) FF, and (d) PCE and SPO of perovskite solar cell devices with a PTAA hole transporting layer measured under various solar concentration factors (up to 128 suns illumination) in air. The device area is $0.87\ cm^2$.



Supplementary Figure 18| Spectral mismatch corrections. **a**, EQE of the perovskite test cell and the KG3 filtered Si reference cell. The specific cells measured here had a J_{sc} of 22.3 mA cm^{-2} . The integrated EQE is 21.2 mA cm^{-2} for both devices. This is within 5% difference which is within the accuracy confidence of the measurements. **b**, Comparison of the measured current of KG3 filtered Si reference cell and the measured power from a power meter when both are illuminated by laser light (532 nm) filtered through each of the neutral density filters. **c**, Spectral mismatch factor between the concentrated solar simulator lamp and the AM1.5G spectrum determined using the perovskite test cell and KG3 filtered Si reference cell shown in (a) when the solar simulator lamp is modulated through neutral density filters with optical densities (OD) between 0 and 3.4. **d**, Comparison of the normalized spectral irradiance of the solar simulator lamp when filtered through each neutral density filter against the AM1.5G standard solar spectrum. The inset shows the specified spectra corresponding to the UV

region. The UV component of the simulated solar spectrum does increase with lower ODs (higher irradiances). Increased UV light should cause more instability problems in perovskite solar cells. Notably, the corresponding spectrum for ~10 suns irradiance, has a similar fraction of UV component to AM 1.5G. e, OD vs suns using the KG3 filtered cell under the simulated sunlight.

Supplementary Note 6. Spectral mismatch factor corrections.

The spectral mismatch between the AM 1.5G standard solar spectrum and the solar simulator lamp was determined for each intensity level, as we show the data in **Supplementary Fig. 18** using a KG3 filtered silicon reference cell. Specifically, the concentrated solar simulator lamp light was passed through an AM 1.5G filter and a neutral density optical filter with optical densities (OD) between 0 and 3.4. The filtered light was collected through an optical fibre equipped with a cosine corrector (Thor Labs) and its spectrum was measured by a Maya Pro (Ocean Optics) spectrometer for each neutral density filter. The background spectrum (*i.e.* when the light path is shuttered) was subtracted from the collected lamp spectrum and the sensitivity of the Maya Pro spectrometer was corrected using a calibrated reference lamp (Oriel). The spectral mismatch of the lamp spectrum to the AM 1.5G spectrum, with respect to the responsivity of our perovskite solar cell, was calculated following the procedure reported previously¹⁹. To correctly determine the equivalent AM1.5G solar light irradiance for each measurement under each neutral density filter, the current density on a KG3 filtered silicon reference cell was measured, and the mismatch factor applied. We note that we ensured that the KG3 filtered silicon reference cell had a linear responsivity to change in light intensity, via measuring the intensity dependence of the short-circuit current density of the KG3 filtered Si reference cell under 532 nm monochromatic laser light, with the intensity of the monochromatic light measured with a thermopile power meter (Gentec-EO).

Supplementary references:

1. Jeon, N. J. *et al.* Solvent engineering for high-performance inorganic-organic hybrid perovskite solar cells. *Nat. Mater.* **13**, 1–7 (2014).
2. Saliba, M. *et al.* Cesium-containing triple cation perovskite solar cells: improved stability, reproducibility and high efficiency. *Energy Environ. Sci.* **9**, 1989–1997 (2016).
3. Kulbak, M. *et al.* Cesium Enhances Long-Term Stability of Lead Bromide Perovskite-Based Solar Cells. *J. Phys. Chem. Lett.* **7**, 167–172 (2016).
4. Noh, J. H., Im, S. H., Heo, J. H., Mandal, T. N. & Seok, S. II. Chemical management for colorful, efficient, and stable inorganic-organic hybrid nanostructured solar cells. *Nano Lett.* **13**, 1764–1769 (2013).
5. Wang, Z. *et al.* Efficient and Air-Stable Mixed-Cation Lead Mixed-Halide Perovskite Solar Cells with n-Doped Organic Electron Extraction Layers. *Adv. Mater.* **29**, 1604186 (2017).
6. Stoumpos, C. C., Malliakas, C. D. & Kanatzidis, M. G. Semiconducting tin and lead iodide perovskites with organic cations: Phase transitions, high mobilities, and near-infrared photoluminescent properties. *Inorg. Chem.* **52**, 9019–9038 (2013).
7. Conings, B. *et al.* Intrinsic Thermal Instability of Methylammonium Lead Trihalide Perovskite. *Adv. Energy Mater.* **5**, 1500477 (2015).
8. Misra, R. K. *et al.* Temperature- and component-dependent degradation of perovskite photovoltaic materials under concentrated sunlight. *J. Phys. Chem. Lett.* **6**, 326–330 (2015).
9. Misra, R. K. *et al.* Effect of Halide Composition on the Photochemical Stability of Perovskite Photovoltaic Materials. *ChemSusChem* **9**, 2572–2577 (2016).
10. Melvin, A. A. *et al.* Lead iodide as a buffer layer in UV-induced degradation of CH₃NH₃PbI₃ films. *Sol. Energy* **159**, 794–799 (2018).
11. Aristidou, N. *et al.* Fast oxygen diffusion and iodide defects mediate oxygen-induced degradation of perovskite solar cells. *Nat. Commun.* **8**, 15218 (2017).
12. Pearson, A. J. *et al.* Oxygen Degradation in Mesoporous Al₂O₃/CH₃NH₃PbI_{3-x}Cl_x Perovskite Solar Cells: Kinetics and Mechanisms. *Adv. Energy Mater.* **6**, 1600014 (2016).
13. McMeekin, D. P. *et al.* A mixed-cation lead mixed-halide perovskite absorber for tandem solar cells. *Science* **351**, 151–155 (2016).
14. Beattie, N. S. *et al.* Analysis of InAs/GaAs quantum dot solar cells using Suns-Voc measurements. *Sol. Energy Mater. Sol. Cells* **130**, 241–245 (2014).
15. Hoke, E. T. *et al.* Reversible photo-induced trap formation in mixed-halide hybrid perovskites for photovoltaics. *Chem. Sci.* **6**, 613–617 (2015).

16. Pockett, A. *et al.* Characterization of planar lead halide perovskite solar cells by impedance spectroscopy, open-circuit photovoltage decay, and intensity-modulated photovoltage/photocurrent spectroscopy. *J. Phys. Chem. C* **119**, 3456–3465 (2015).
17. Newville, M., Ingargiola, A., Stensitzki, T. & Allen, D. B. LMFIT: Non-Linear Least-Square Minimization and Curve-Fitting for Python. *Astrophys. Source Code Libr.* ascl:1606.014 (2016).
18. Christoforo, M. G. Batch IV Analysis. Available at: <https://github.com/greysAcademicCode/batch-iv-analysis>.
19. Snaith, H. J. How should you measure your excitonic solar cells? *Energy Environ. Sci.* **5**, 6513 (2012).